Int. J. Advanced Design and Manufacturing Technology, 2023, Vol. 16, No. 4, pp. 87-97

DOI: 10.30495/ADMT.2022.1949929.1334 ISSN: 2252-0406 https://admt.isfahan.iau.ir

Investigation of Pressure Distribution on Slippers of a Monorail Sled with Vibration Damper

Mohammad Reza Najafi
Department of Mechanical Engineering,
University of Imam Hossein Comprehensive, Iran
E-mail: drmrnajafi@ihu.ac.ir

Saeed Mahjoub Moghadas *
Department of Mechanical Engineering,
University of Imam Hossein Comprehensive, Iran
E-mail: smahjoubmoghadas@ihu.ac.ir
*Corresponding author

Received: 15 January 2022, Revised: 3 April 2022, Accepted: 15 April 2022

Abstract: In this paper, the pressure distribution on the slippers of a mono-rail sled with vibration damping is investigated. Due to the many applications of sled testing in the aerospace industry, the study of system vibrations is highly noticeable. In this research, first, by mathematical modelling of the sled, the governing Equations are extracted and natural frequencies and vibration modes are obtained from the analytical method using the mass and stiffness matrix of the system. Then, using numerical simulation and validation methods with experimental results performed in wind tunnels, the modal analysis of the designed sled sample is performed. A difference of less than eight percent in both numerical and analytical methods proves the accuracy of the results. The results show that the role of the slipper in the vibrations created in the sled is very important due to the large torsional and transverse oscillations in different positions, and the highest static pressure occurs in the inner layer of the slipper.

Keywords: Modal Analysis, Natural Frequency, Pressure Distribution, Sled Test, Slipper

Biographical notes: Mohammad Reza Najafi received his PhD in Mechanical Engineering from Imam Hossein Comprehensive University in Tehran, Iran. His current research interests include vibration and dynamics. **Saeed Mahjoub Moghadas** is an Associate Professor of Mechanical engineering at the University of Imam Hossein Comprehensive, Iran, since 1986. He received his PhD with the thesis subject "Internal Combustion Engines Control and Diagnostics through Instantaneous Speed of Rotation Analysis" at L'ensam University, Paris, France, in 1985. He has authored 20 books and translated 15 others in the field of dynamic, vibration, and control.

Research paper

1 INTRODUCTION

Sled testing technology is now limited to a few countries. Experimental facilities of this technology include long rails, chassis, carriage, propulsion engines, and sled or projectile body. Slippers are used to connect this system to the rails. The slippers slide on the rails to allow the sled to move. Fig. **1** shows how to connect rail and slipper.

Fig. 1 Sled and rail connection.

The sled technology is used to achieve supersonic speeds up to 8 Mach and to provide experimental conditions in the field of space equipment [1], projectile penetration [2], parachute [3], pilot seat [4], anti-penetration structures [5], propulsion tests [6], and ultrasonic aerodynamic tests [7]. Real examples of sleds are also shown in "Fig. 2".

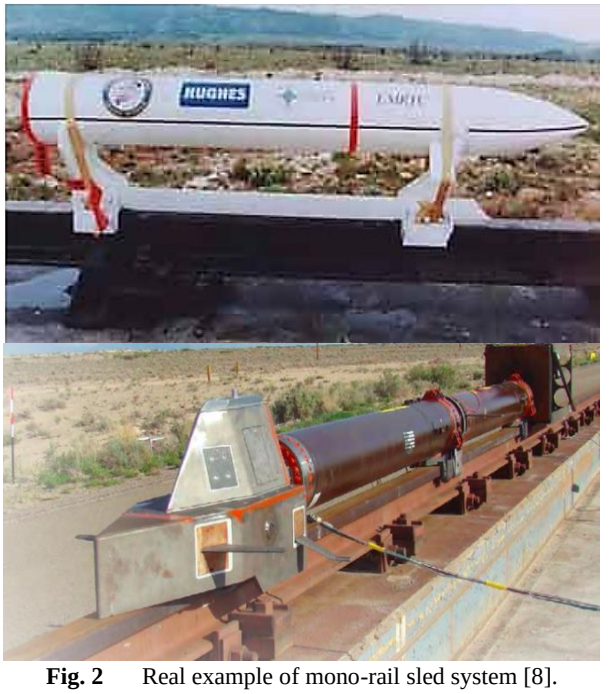

Fig. 2 Real example of mono-rail sled system [8].

Sled testing technology has attracted the attention of researchers in recent years [9–13]. Due to the high speed of this technology, the vibrations on the sled are one of the main bottlenecks of this system, which has been noticed by many researchers [14–17]. Minto discussed a sled capacity development program to achieve high supersonic speeds. The results of their research show that the generated vibrational loads due to the impact of the slipper on the rail at speeds more than 6000 ft/sec lead to the failure of the sled body [18]. Bosmajian et al. studied the magnetic rail system of the sled. The aim of this study was to increase the sled capability for reduction of the vibrational environment at a final speed of 3000 m/s [19], and in the continuation of this research, Gurol et al. investigated the condition of the magnetic rail track in sled test at a higher speed. They showed that using a magnetic suspension system could significantly reduce sled vibrations [20]. Chen et al. investigated the amplitude of rocket sled vibrations and the time and frequency measurements of irregularity characteristics using statistical methods [21]. Turnbull et al. investigated the dynamic analysis of a sled system using narrow-gauge rails. The aerodynamic parameters of drag and lift, and pitch and yaw torques have been studied as a function of the angle of attack and acceleration has been obtained at four points on the sled [22]. Dunshee has modeled the mono-rail sled system as a two-degree-of-freedom beam with the capability to twist slightly in addition to moving in a vertical direction, using dynamic and vibrational analysis, and also has assumed the dynamic movement and a harmonic stimulation of a slipper [23]. Researchers have used mathematical models such as beams to analyze the behavior of dynamic systems such as high-speed trains, bridges, and automobiles [24–27]. Afshar et al. modelled the train bridge as a beam and investigated the use of linear and nonlinear vibration dampers for nonlinear beams at transient loads. The results show that for normal forces and short beams, linear and nonlinear models have similar behaviors [28].

Despite the research that has been done on sled testing, vibration analysis and modal analysis of sleds considering study of the role and the pressure distribution on slipper, which are the main outstanding of the present paper, have not been carried out by researchers so far. In the present paper, using the analytical method, first the vibrational Equations of the system are extracted and the natural frequencies are obtained. Then, the numerical simulation method is used to validate the obtained results and the modal analysis of a mono-rail sled with dampers is performed and the shape of its modes is clarified. Finally, the pressure and velocity distributions in the computational domain and the body of the sled and the slippers are also examined.

2 MATHEMATICAL MODELING

Most of the sled vibrations are caused by the impact of the slippers on the rails. Since the materials used in sleds and slippers are stiff, considerable vibrations are transmitted from the slippers and the rails to the body due to the impact of the rails [29], most of which occur in the upper parts of the slipper [30]. Thus, the use of dampers at the junction of the sled body to the slipper can greatly prevent the transmission of vertical vibrations from the rail surface to the sled. In this case, the sled can be modeled as a system that is excited transversely from the slipper. An overview of this type of sled modeling is shown in "Fig. 3".

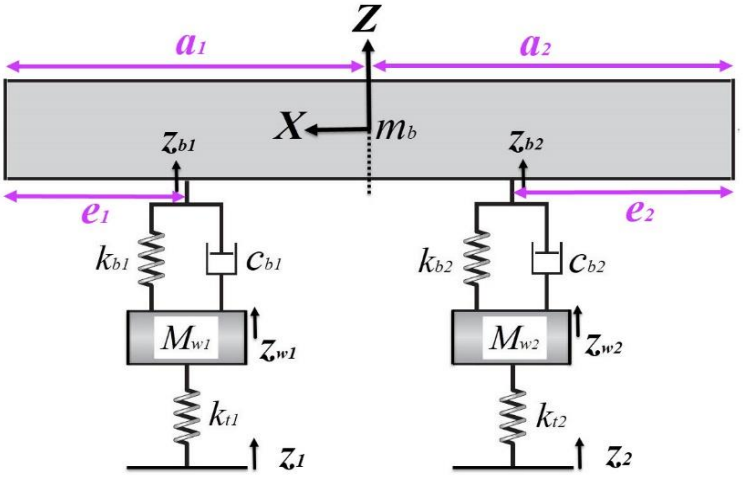

Fig. 3 Sled mathematical model.

The parameters of present modeling describe m_b as sled body mass, m_{w1} as front slipper mass, m_{w2} as rear slipper mass, z_b as vertical sled body displacement, z_{b1} as rear slipper displacement, z_{b2} as rear slipper displacement, θ_b as a rotation of sled body around Y-axis (pitch motion) and I_{yy} as inertia moment.

3 EXTRACTIONS OF GOVERNING EQUATIONS

Considering the displacement of the slippers due to the transverse motion of the center of mass as well as the twisting motion around the Y-axis (θ_b), there is:

$$z_{b1} = z_b - (a_1 - e_1)\,\theta_b \tag{1}$$

$$\dot{z}_{b1} = \dot{z}_b - (a_1 - e_1)\,\dot{\theta}_b \tag{2}$$

$$z_{b2} = z_b + (a_2 - e_2)\,\theta_b \tag{3}$$

$$\dot{z}_{b2} = \dot{z}_b + (a_2 - e_2)\,\dot{\theta}_b \tag{4}$$

So, the vibrational Equations of the various components of the sled are now being extracted. To move the front slipper, there is m_{w1} in the Z direction as obtained in relation (5):

$$\begin{aligned} &m_{w1}\ddot{z}_{w1} - k_{b1}\left(z_b - (a_1 - e_1)\theta_b - z_{w1}\right) \\ &-c_{b1}\left(\dot{z}_b - (a_1 - e_1)\dot{\theta}_b - \dot{z}_{w1}\right) \\ &-k_{t1}\left(z_{w1} - z_1\right) = 0 \end{aligned} \tag{5}$$

For the rear slipper motions, there is m_{w2} in the Z direction as discussed in the relation (6):

$$\begin{aligned} &m_{w2}\ddot{z}_{w2} - k_{b2}\left(z_b + (a_2 - e_2)\,\theta_b - z_{w2}\right) \\ &-c_{b2}\left(\dot{z}_b + (a_2 - e_2)\,\dot{\theta}_b - \dot{z}_{w2}\right) \\ &-k_{t2}\left(z_{w2} - z_2\right) = 0 \end{aligned} \tag{6}$$

For the sled body motion (m_b) in the Z direction, there is:

$$\begin{aligned} &m_b\ddot{z}_b + k_{b1}\left(z_b - (a_1 - e_1)\,\theta_b - z_{w1}\right) + \\ &c_{b1}\left(\dot{z}_b - (a_1 - e_1)\,\dot{\theta}_b - \dot{z}_{w1}\right) + \\ &k_{b2}\left(z_b + (a_2 - e_2)\,\theta_b - z_{w2}\right) + \\ &c_{b2}\left(\dot{z}_b + (a_2 - e_2)\,\dot{\theta}_b - \dot{z}_{w2}\right) = 0 \end{aligned} \tag{7}$$

For the sled body rotation around the Y-axis, there is:

$$\begin{aligned} &I_{yy}\ddot{\theta}_b - k_{b1}\left(z_b - (a_1 - e_1)\,\theta_b - z_{w1}\right)(a_1 - e_1) \\ &- c_{b1}\left(\dot{z}_b - (a_1 - e_1)\,\dot{\theta}_b - \dot{z}_{w1}\right)(a_1 - e_1) \\ &+ k_{b2}\left(z_b + (a_2 - e_2)\,\theta_b - z_{w2}\right)(a_2 - e_2) \\ &+ c_{b2}\left(\dot{z}_b + (a_2 - e_2)\,\dot{\theta}_b - \dot{z}_{w2}\right)(a_2 - e_2) = 0 \end{aligned} \tag{8}$$

By multiplying the above values as indicated in relation (8), and simplifying them, the vibrational Equations of the four-degree-of-freedom system are obtained.

$$\begin{aligned} &m_{w1}\,\ddot{z}_{w1} + c_{b1}\,\dot{z}_{w1} - c_{b1}\,\dot{z}_b + S_{13}\,\dot{\theta}_b + \\ &k_{b1}\,z_{w1} - k_{b1}\,z_b + S_{12}\,\theta_b = 0 \end{aligned} \tag{9}$$

$$\begin{aligned} &m_{w2}\,\ddot{z}_{w2} + c_{b2}\,\dot{z}_{w2} - c_{b2}\,\dot{z}_b - S_{15}\,\dot{\theta}_b + \\ &k_{b2}\,z_{w2} - k_{b2}\,z_b - S_{14}\,\theta_b = 0 \end{aligned} \tag{10}$$

$$\begin{aligned} &m_b\,\ddot{z}_b - c_{b1}\,\dot{z}_{w1} - c_{b2}\,\dot{z}_{w2} + S_{23}\,\dot{z}_b - \\ &S_{25}\,\dot{\theta}_b - k_{b1}\,z_{w1} - k_{b2}\,z_{w2} + S_{22}\,z_b - \\ &S_{24}\,\theta_b = 0 \end{aligned} \tag{11}$$

$$\begin{aligned} &I_{yy}\,\ddot{\theta}_b + S_{13}\,\dot{z}_{w1} - S_{15}\,\dot{z}_{w2} - S_{25}\,\dot{z}_b + \\ &S_{27}\,\dot{\theta}_b + S_{12}\,z_{w1} - S_{14}\,z_{w2} - S_{24}\,z_b + \\ &S_{26}\,\theta_b = 0 \end{aligned} \tag{12}$$

In the above Equations, the parameters are introduced as follows:

$$k_{b1}(a_1 - e_1) = S_{12} \tag{13}$$

$$c_{b1}(a_1 - e_1) = \dot{S}_{13} \tag{14}$$

$$k_{b2}(a_2 - e_2) = S_{14} \tag{15}$$

$$c_{b2}(a_2 - e_2) = \dot{S}_{15} \tag{16}$$

$$k_{b1}(a_1 - e_1)^2 = S_{12}(a_1 - e_1) = S_{16} \tag{17}$$

$$c_{b1}(a_2 - e_2)^2 = \dot{S}_{13}(a_1 - e_1) = \dot{S}_{17} \tag{18}$$

$$k_{b2}(a_1 - e_1)^2 = S_{14}(a_2 - e_2) = S_{18} \tag{19}$$

$$c_{b2}(a_2 - e_2)^2 = \dot{S}_{15}(a_2 - e_2) = \dot{S}_{19} \tag{20}$$

$$k_{b1} + k_{b2} = S_{22} \tag{21}$$

$$c_{b1} + c_{b2} = \dot{S}_{23} \tag{22}$$

$$S_{12} - S_{14} = S_{24} \tag{23}$$

$$\dot{S}_{13} - \dot{S}_{15} = \dot{S}_{25} \tag{24}$$

$$S_{16} + S_{18} = S_{26} \tag{25}$$

$$\dot{S}_{17} + \dot{S}_{19} = \dot{S}_{27} \tag{26}$$

$$k_{t1}(z_{w1} - z_1) = f_{w1} \tag{27}$$

$$k_{t2}(z_{w2} - z_2) = f_{w2} \tag{28}$$

That Equation of system motions is obtained as relation (29):

$$[M]\,\ddot{z} + [C]\,\dot{z} + [K]\,z = F \tag{29}$$

Thus, the Equations of vibrational motion of the system are obtained as relation (30):

$$\begin{aligned} &\begin{bmatrix} m_b & 0 & 0 & 0 \\ 0 & I_{yy} & 0 & 0 \\ 0 & 0 & m_{w1} & 0 \\ 0 & 0 & 0 & m_{w2} \end{bmatrix} \begin{bmatrix} \ddot{z}_b \\ \ddot{\theta}_b \\ \ddot{z}_{w1} \\ \ddot{z}_{w2} \end{bmatrix} \\ &+ \begin{bmatrix} \dot{S}_{23} & -\dot{S}_{25} & -c_{b1} & -c_{b2} \\ -\dot{S}_{25} & \dot{S}_{27} & \dot{S}_{13} & -\dot{S}_{15} \\ -c_{b1} & \dot{S}_{13} & c_{b1} & 0 \\ -c_{b2} & -\dot{S}_{15} & 0 & c_{b2} \end{bmatrix} \begin{bmatrix} \dot{z}_b \\ \dot{\theta}_b \\ \dot{z}_{w1} \\ \dot{z}_{w2} \end{bmatrix} \\ &+ \begin{bmatrix} S_{22} & -S_{24} & -k_{b1} & -k_{b2} \\ -S_{24} & S_{26} & S_{12} & -S_{14} \\ -k_{b1} & S_{12} & k_{b1} & 0 \\ -k_{b2} & -S_{14} & 0 & k_{b2} \end{bmatrix} \begin{bmatrix} z_b \\ \theta_b \\ z_{w1} \\ z_{w2} \end{bmatrix} = \begin{bmatrix} 0 \\ 0 \\ f_{w1} \\ f_{w2} \end{bmatrix} \end{aligned} \tag{30}$$

According to the modeling of a mono-rail sled, mass values and geometry of different components were extracted. The amount of elastomer stiffness used on top of the slipper was also obtained experimentally. “Table 1” shows the values of the various parameters of the designed sled.

Table 1 The values of the various parameters of the designed sled [31]

Parameter	Values	Unit
m_b	14.69	kg
$m_{w1} = m_{w2}$	0.79	kg
$k_{b1} = k_{b2}$	370	kN/m
$C_{b1} = C_{b2}$	29.94	N.s/m
a_1	450	mm
a_2	393	mm
e_1	285	mm
e_2	195	mm

4 RESULTS

Vibrational analysis and sled modal analysis need to be carried out numerically and the numerical simulation results must be verified before numerical simulation of the sled is done.

4.1. Validation of Numerical Results

In terms of the aerodynamic geometry of the sleds, a study is done in which the drag force of an Ogive body is obtained experimentally in the NASA wind tunnel of the United States. In addition to the advantage of presenting experimental results, the model has no wings and is geometrically similar to the sled in this study.
For validation, an Ogive cylinder body is simulated according to the test conditions using computational fluid dynamics methods and the drag force is calculated. To extract the values related to the Ogive nose in the experimental work, first, according to “Fig. 4”, the following relations were used.

$$y = \sqrt{\rho^2 - (L - x)^2} + R - \rho \quad (31)$$

$$\rho = \frac{R^2 + L^2}{2R} \quad (32)$$

For the nose profile relations, the following values are placed and the y parameter is calculated for different x parameters.

$$L = 14 \text{ in.}, R = 2 \text{ in.} \Rightarrow \rho = 50 \text{ in.} \quad (33)$$

$$y = \sqrt{2500 - (14 - x)^2} - 48[in.] \quad (34)$$

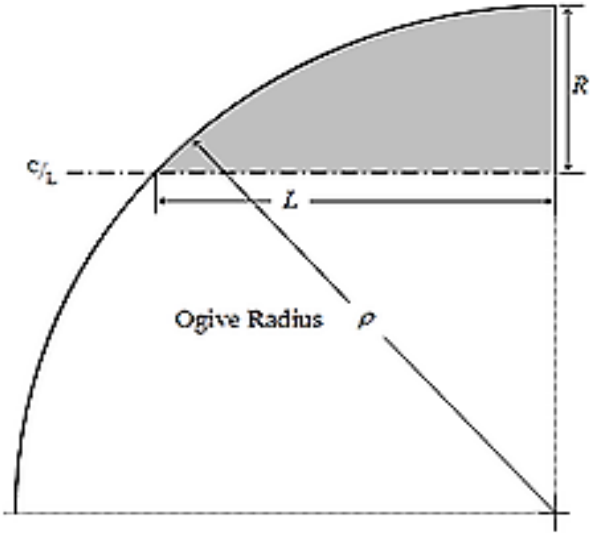

Fig. 4 Measurement with parameters of Ogive nose.

Considering the obtained values, “Fig. 5” is represented.

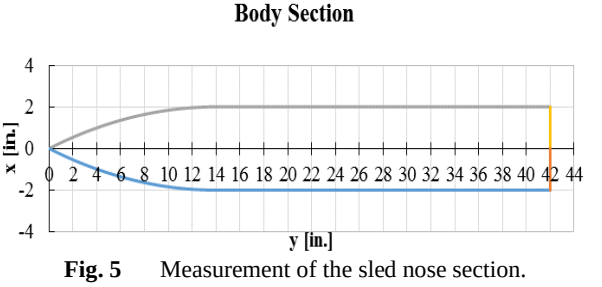

Fig. 5 Measurement of the sled nose section.

Then, the Ogive nose is designed, which is shown in “Fig. 6”.

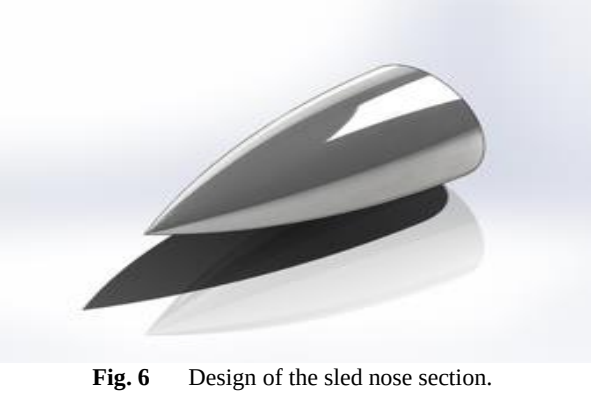

Fig. 6 Design of the sled nose section.

The body geometry is designed using the model specifications shown in “Fig. 7”.

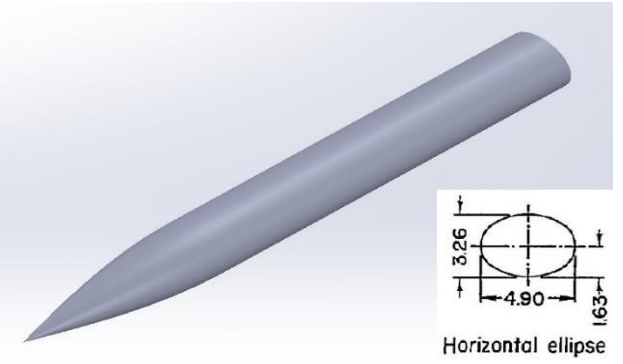

Fig. 7 Geometry of model regarding [32].

The computational field and the network around the model are taken into consideration using the software and the range of fluid flow is analyzed. The dimensions of the domain should be considered large enough that it does not affect the results. ("Fig. 8").

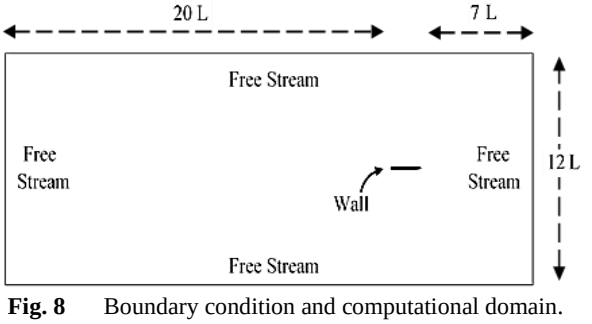

Fig. 8 Boundary condition and computational domain.

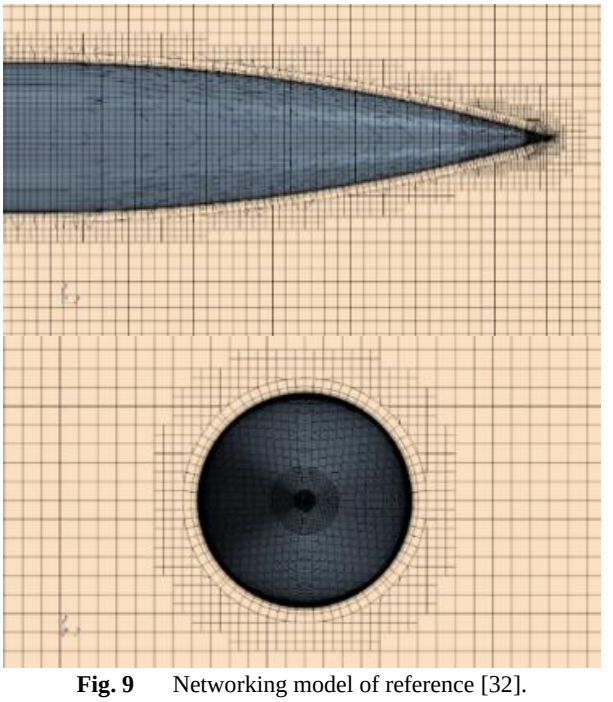

Fig. 9 Networking model of reference [32].

In this study, the length of the calculated range is 28 times more than the length of the body, so the distance from the beginning of the domain range to the nose portion is 7 times more than the length, and the distance from the end of the body to the end of the domain is 20 times more than it. The width and height of the domain are also 12 times more than the length. In all cases, for all boundaries around the domain, a freestream boundary condition was applied. The mesh networking of the model is produced using the trimmer method, which has four rows of boundary layers, the number of cells is 2707757 and the total thickness of the boundary layer network is 0.0072 m. Fig. **9** shows the research networking of the aforementioned reference. The side view and the front view of the meshing in the whole computational range are also shown in "Fig. 10".

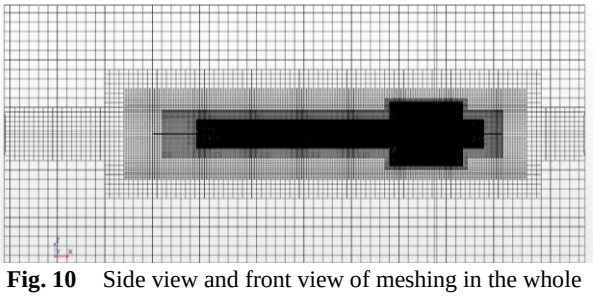

Fig. 10 Side view and front view of meshing in the whole computational range.

In all simulations, the k-ε model is selected, which is suitable for engineering problems with high Reynolds numbers. In the k-ε model, the Y^+ boundary layer network must be greater than 30 and less than 300, as "Fig. 11" confirms.

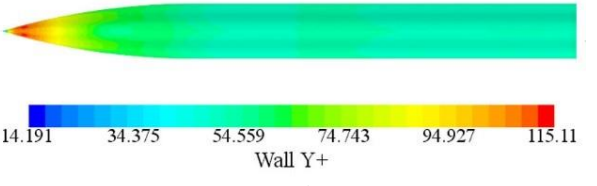

Fig. 11 Y^+ values.

The amount of drag force in the present numerical method in comparison with the amount of drag force obtained from the experimental test at two different cross-sectional levels and pressures is given in "Table 2".

Table 2 Comparison of numerical and experimental simulation results

P_0 [psi]	Experimental results [N]	Present working [N]	Error percent
7.5	64.76	59.23	8.54
4.5	40.39	36.8	8.88

The results show that the error of the numerical method is less than 10% of the experimental test results, so the results of the numerical simulation method in the present study are confirmed.

4.2. Numerical Simulation

Considering the accuracy of the numerical solution methods, the numerical analysis of the sled is carried out. The studied sled in the present study is integrated and due to the mono-rail option, it lacks chassis and carriage. Dimensions and computational domain meshing, coordinate system and boundary conditions were carried out regarding the validation model of [32]. The computational domain and meshing network around the body are shown in "Fig. 12" from the front view. The mesh number in the computational domain is 2846662.

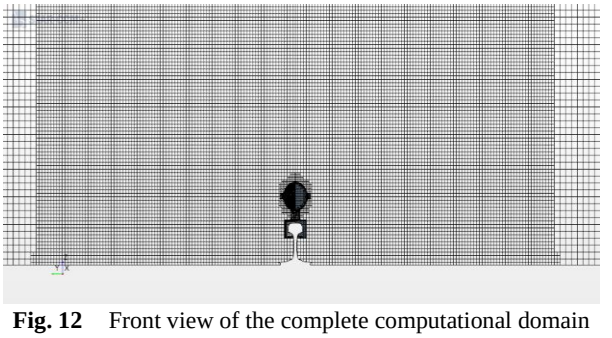

Fig. 12 Front view of the complete computational domain meshing.

The simulation settings were considered to be the same as the validation. The properties of the working fluid are shown in "Table 3".

Table 3 Working fluid properties and environmental conditions [33].

Parameter	Values	Unit
P_0	101325	Pa
T_0	288.15	K
c	340.3	$\frac{m}{s}$
μ	1.789×10^{-5}	$\frac{kg}{m.s}$
ρ	1.225	$\frac{kg}{m^3}$

The sled model of the present study is finally shown in "Fig. 13".

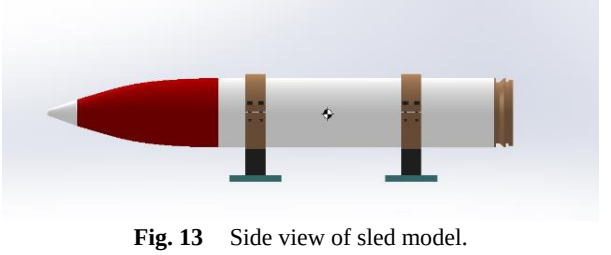

Fig. 13 Side view of sled model.

4.3. Modal analysis

For multi-degree-of-freedom systems, matrices and vectors are used to determine modal properties, and to extract natural frequencies. The Equation of motion of the system is considered as relation (35):

$$[\mathrm{M}]\left\{\ddot{\mathrm{z}}(\mathrm{t})\right\}+[\mathrm{C}]\left\{\dot{\mathrm{z}}(\mathrm{t})\right\}+[\mathrm{K}]\left\{\mathrm{z}(\mathrm{t})\right\}=\{\mathrm{F}\} \quad (35)$$

Also, there is:

$$\{\Psi\}_r=\{z(t)\}=\{Z\}e^{i\omega t} \quad (36)$$

Considering Equation (36), to investigate the motion of free vibrations of the sled system, there is relation (37):

$$\left([K]-\boldsymbol{\omega}^2[M]\right)\{\boldsymbol{\Psi}\}=\{0\} \quad (37)$$

Considering orthogonality of modes, there is:

$$\omega_r{}^2=\frac{k_r}{m_r},\ (r=1,2,...,n) \quad (38)$$

In the above relations, m_r and k_r are related to the mass and stiffness of the modal or the generalized mass and stiffness of the r^{th} mode. [Kr] and [Mr] are considered as the mass and stiffness matrices for the r^{th} mode respectively, so the natural frequency and the mode shape matrices can be written as (39) and (40):

$$\left[\omega_r^2\right]=\begin{bmatrix}\omega_1^2 & 0 & ... & 0\\ 0 & \omega_2^2 & ... & 0\\ ... & ... & ... & ...\\ 0 & 0 & ... & \omega_n^2\end{bmatrix} \quad (39)$$

$$[\Psi]=\left[\{\Psi\}_1,\{\Psi\}_2,...,\{\Psi\}_n\right] \quad (40)$$

The Equation of motion of a multi-degree-of-freedom system with disproportionate structural damping is expressed as relation (41):

$$[M]\left\{\ddot{x}\right\}+[K]\{x\}+i\left[C^*\right]\{x\}=\{0\} \quad (41)$$

The damping structure matrix can be considered as an imaginary part of a complex stiffness matrix, defined as relation (42):

$$\left[K^*\right]_c=[K]+i\left[C^*\right] \quad (42)$$

To solve the above Equation, relation (43) is obtained:

$$\{x(t)\} = \{X\}\ e^{j\lambda t} \tag{43}$$

In this relation, λ is a complex frequency and includes both vibration and damping terms, and {X} indicates the complex vector of displacement domains. By substituting the value, the following problem of complex eigenvalue is obtained as the following relation.

$$\left(\left[K^*\right]_c - \lambda^2[M]\right)\{X\} = \{0\} \tag{44}$$

The solution of Equation (44) includes the diametric matrix of the eigenvalue [λr] and the eigenvector matrix [Ψ]. The relation of the eigenvalue λr^2 with the natural frequency ω_r and the damping dissipation coefficient of the system ηr is obtained as relation (45):

$$\lambda_r^{\ 2} = \omega_r^{\ 2}\left(1 + i\eta_r\right)\ ,\ (r = 1, 2, ..., n) \tag{45}$$

λr is known as the complex natural frequency of the system. [λr^2] is the natural frequency matrix of the system. The corresponding eigenvector, $\{\Psi\}_r$, is a complex vector. All eigenvectors, corresponding eigenvalues of ω_r in ascending order, are placed next to each other and these values result in the mixed matrix as the mode shape matrix of [Ψ]. Considering the orthogonal properties of the system, there is:

$$\left[\lambda_r^{\ 2}\right] = \left[m_r\right]^{-1}\left[k_r\right] \tag{46}$$

In this case, the modal mass of m_r and the modality stiffness of k_r are complex values. To obtain natural frequencies, given the four degrees of freedom of the system, [λr^2] value for the four modes of the system is considered equal to the matrix of [B].

$$[B] = [M]^{-1}\ [K] \tag{47}$$

By placing the value of $[m_r]^{-1}$ in Equation (46) and obtaining the root mean square of the eigenvalues, the natural frequencies of the system will be in the form of a matrix of [λr].

$$\lambda_r = \begin{Bmatrix} 84.7 & rad/s \\ 129.9 & rad/s \\ 866.5 & rad/s \\ 855.1 & rad/s \end{Bmatrix} \cong \begin{Bmatrix} 13.48 & Hz \\ 20.68 & Hz \\ 137.9 & Hz \\ 136.1 & Hz \end{Bmatrix} \tag{48}$$

Finally, the system modes are obtained as follows:

$$u_1 = \begin{bmatrix} 0 \\ 0.99 \\ -0.11 \\ 0.11 \end{bmatrix},\ u_2 = \begin{bmatrix} -0.73 \\ 0 \\ -0.48 \\ -0.48 \end{bmatrix}$$
$$u_3 = \begin{bmatrix} 0.05 \\ 0 \\ -0.71 \\ -0.71 \end{bmatrix},\ u_4 = \begin{bmatrix} 0 \\ 0.12 \\ 0.7 \\ -0.7 \end{bmatrix} \tag{49}$$

Where, the first and second modes indicate torsional and transverse vibrations of the system, respectively. The third and fourth modes show the vertical vibrations of both slippers and the vibrational motion due to torsion, respectively. The transverse and torsional vibrations of all modes demonstrate the importance of the slipper role in the sled system.

To validate the values of the natural frequencies of the system analytically and to obtain the shape of the modes, a modal analysis of the designed sled is carried out numerically. The mesh model of the designed sled is shown in "Fig. 14".

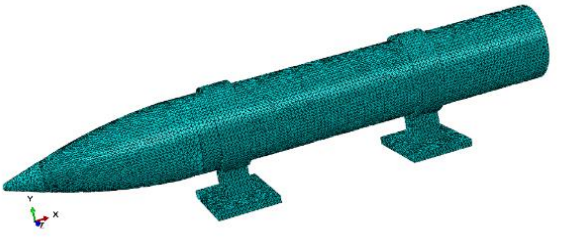

Fig. 14 Meshing of designed sled model.

Fig. **15** shows the sled modal analysis for the first mode of the system which is related to the torsional vibration around the center of mass of the sled. Due to the rigidity of the sled body, the amount of torsional vibration is low.

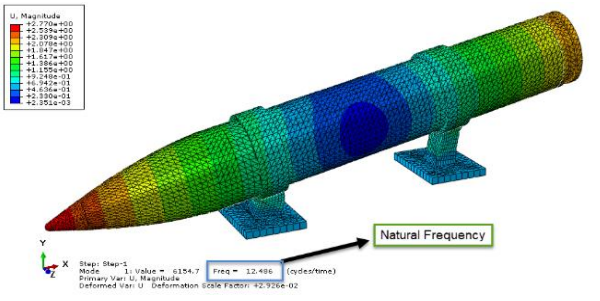

Fig. 15 First (torsional) mode of sled.

Fig. **16** shows the second mode, which shows the transverse vibrations of the sled. In this case, the sled vibrates vertically without torsional motion, and the vibration rate of the two slippers is equal to each other.

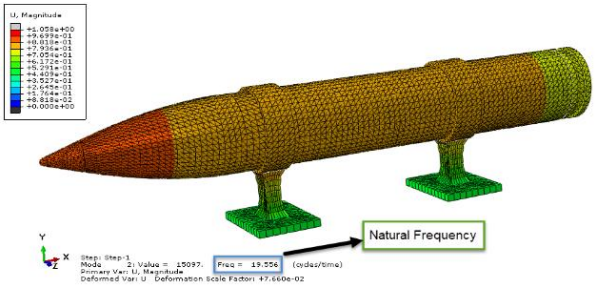

Fig. 16 Second (transverse) mode of the sled.

In the third mode, both slippers vibrate in one direction (transverse) and there is no torsional movement in the sled as shown in "Fig. 17". The vibrations are much greater than the first and second vibrations modes which implies the importance of the slipper role in the sled system.

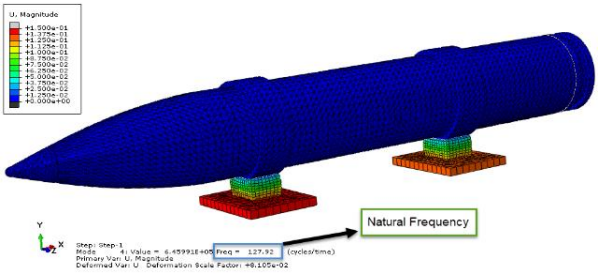

Fig. 17 Third mode of the sled.

The fourth mode is similar to the third mode, except that the displacement of slippers is in opposite directions due to torsional vibrations. Fig. **18** represents the fourth mode.

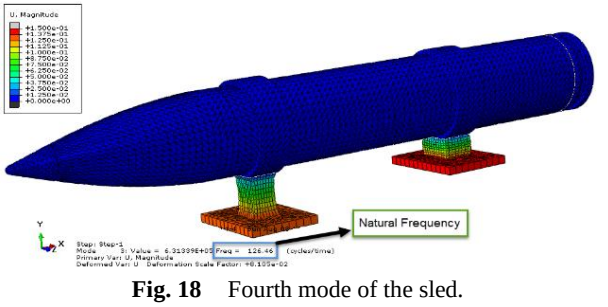

Fig. 18 Fourth mode of the sled.

"Table 4" describes the values of the natural frequencies of the system in both analytical and numerical methods. The results error is less than 8%, and both results are confirmed. The difference in results can be attributed to the distribution of mass and geometry of the sled. On the other hand, the obvious difference between the frequencies of the first and second modes from the frequencies of the third and fourth modes shows the significant role of the slipper in the sled system.

Table 4 Comparison of natural frequencies in numerical simulation method with analytical method

Natural frequency	Numerical result (Hz)	Analytical result (Hz)	Error percentage
First mode	12.49	13.48	7.34
Second mode	19.56	20.68	5.41
Third mode	127.9	137.9	7.25
Forth mode	126.5	136.1	7.42

4.4. Pressure and Velocity Distribution

Fig. **19** shows the contour of the Mach number in the computational domain. According to the velocity distribution, it is assumed that a vortex is formed due to the pressure difference in the back of the sled body. Also, the highest pressure after the front slipper is applied on the distance part between the two slippers.

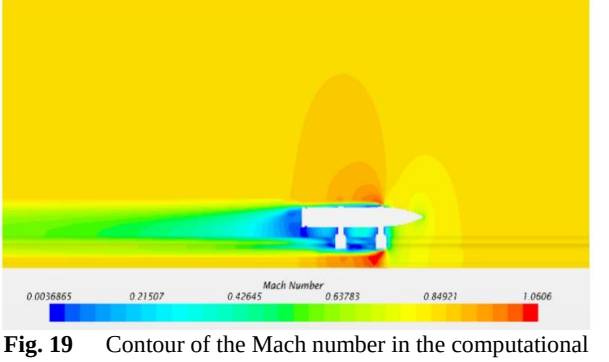

Fig. 19 Contour of the Mach number in the computational domain.

Fig. **20** shows the high-pressure areas of the fluid around the sled. As can be seen, the highest pressure, except the front slipper, is in the distance between the two slippers.

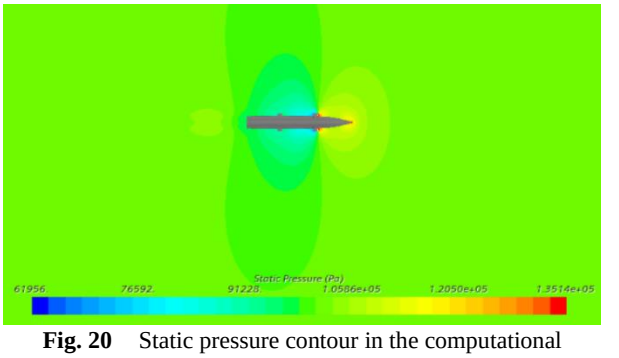

Fig. 20 Static pressure contour in the computational domain.

5 CONCLUSIONS

In this paper, the pressure distribution on the slippers of a mono-rail sled has been investigated, and the vibrational and modal analyses are also investigated with an emphasis on the role of slippers. First, the governing vibration Equations, natural frequencies of the system, and vibration modes were extracted in the analytical method. Then, by validating the numerical method with the experimental results performed in the wind tunnel, modal analysis of sled system was carried out, and the modes shapes were designed. The torsional and transverse vibrations created in the slippers as well as the static pressure distribution of the slippers show that this part of the sled, which has more risk of damage due to applied stresses, is very important.

REFERENCES

[1] Gragossian, A., Pierrottet, D. F., Estes, J., Barnes, B. W., Amzajerdian, F., and Hines, G. D., Navigation Doppler Lidar Performance Analysis at High Speed and Long Range, AIAA Scitech 2020 Forum 1 PartF(January), 2020, pp. 1–6. Doi: 10.2514/6.2020-0369.

[2] Deleon, A., Baker, W. P., and Palazotto, A. N., Evaluation of a Nonlinear Melt Region Produced Within a High Speed Environment, AIAA/ASCE/AHS/ASC Struct Struct Dyn Mater Conf 2018 (210049), 2018, pp. 1–17. Doi: 10.2514/6.2018-0187.

[3] Meacham, M. B., Gallon, J. C., Johnson, M. R., Natzic, D. B., Thompson, N., Aguilar, D., Marti, B., Hennings, E., and Rivellini, T., Rocket Sled Strength Testing of Large, Supersonic Parachutes, Aerodyn Decelerator Syst Technol Conf1–28, 2015. Doi: 10.2514/6.2015-2163.

[4] Guan, H., Zhu, Y., and Zhang, S. J., Aerodynamic characteristics of Ejection Seat and Occupant, 51st AIAA Aerosp Sci Meet Incl New Horizons Forum Aerosp Expo 2013 (January), 2013, pp. 1–20, Doi: 10.2514/6.2013-386.

[5] Cinnamon, J. D., Palazotto, A. N., Further Validation of A General Approximation for Impact Penetration Depth Considering Hypervelocity Gouging Data, Int J Impact Eng, Vol. 34, No. 8, 2007, pp. 1307–1326. Doi: 10.1016/j.ijimpeng.2006.08.005.

[6] Nakata, D., Kozu, A., Yajima, J., Nishine, K., Higashino, K., and Tanatsugu, N., Predicted and Experimented Acceleration Profile of the Rocket Sled, Trans Japan Soc Aeronaut Sp Sci Aerosp Technol Japan 10(ists28):Ta_1-Ta_5, 2012. Doi: 10.2322/tastj.10.ta_1.

[7] Xiao, J., Zhang, W. W., Xue, Q., Zhang, L. R., and Zhou, X. B., Reliability Analysis of Engine Shell Strength under Rocket Sledge Vibration Environment, J Phys Conf Ser, Vol. 1176, No. 6, 2019, pp. 4–9, Doi: 10.1088/1742-6596/1176/6/062047.

[8] Butova, S. V., Gerasimov, S. I., Erofeev, V. I., and Kamchatnyi, V. G., Stability of High-Speed Objects Moving Along a Rocket Track Guide. J Mach Manuf Reliab, Vol. 44, No. 1, 2015, pp. 1–5. Doi: 10.3103/S1052618815010021.

[9] Hooser, C., Afb, H., and Beach, H., AIAA 2002-3037 AIAA 2002-3037 Proposed Hypersonic Air-Breathing Test Capability At The Holloman High Speed Test Track Usaf-Holloman High Speed Test Track Neil Bosmajian The Boeing Company-Reusable Space Systems, Test (June), 2002, pp. 1–12.

[10] Nakata, D., Yajima, J., Nishine, K., Higashino, K., Tanatsugu, N., and Kozu, A., Research and Development of High Speed Test Track Facility in Japan. 50th AIAA Aerosp Sci Meet Incl New Horizons Forum Aerosp Expo (January), 2012, pp. 1–11. Doi: 10.2514/6.2012-928.

[11] Hsu, Y. H., Langhorn, A., Ketchen, D., Holland, L., Minto, D., and Doll, D., Magnetic Levitation Upgrade to the Holloman High Speed Test Track, IEEE Trans Appl Supercond, Vol. 19, No. 3, 2009, pp. 2074–7. Doi: 10.1109/TASC.2009.2019558.

[12] Kumar, V., Terrazas, J., Edmonds, R., and Kotteda, V. M. K., Multiphase CFD Modeling of The Braking Phenomena for The Holloman High-Speed Test Track, 23rd AIAA Int Sp Planes Hypersonic Syst Technol Conf 2020, 2020, pp. 1–10. Doi: 10.2514/6.2020-2446.

[13] Wang, B., Zheng, J., Yu, Y., Lv, R., and Xu, C., Shock-Wave/Rail-Fasteners Interaction for Two Rocket Sleds in The Supersonic Flow Regime, Fluid Dyn Mater Process, 2020. Doi: 10.32604/FDMP.2020.09681.

[14] Guangqi, H., Yin, A. I., R., and Zhenzhen, J., Simulation Analysis of Rocket Sled Vibration Reduction Platform, J Exp Test, Vol. 2, 2006, pp. 10–3.

[15] Xiao, J., Zhang, W. W., Xue, Q., Gao, W. B., and Deng, B., Analysis of Rocket Sled Vibration Signal Transmission Based on Zigbee Application, J Phys Conf Ser, Vol. 1176, No. 6, 2019, pp. 8–13. Doi: 10.1088/1742-6596/1176/6/062006.

[16] Tong, D. C., Mechanical Simulation of Rocket Sled Test Damping System, Nav Electron Eng, Vol. 8, 2012, pp. 87–9.

[17] Compilation, D. W., Theory of Vibration Reduction, Tsinghua Univ Press, 2014, pp. 69–91.

[18] Minto, D. W., Recent Increases in Hypersonic Test Capabilities at the Holloman High Speed Test Track, 38th Aerosp Sci Meet Exhib (January), 2000. Doi: 10.2514/6.2000-154.

[19] Bosmajian, N., Minto, D., and Holland, L., Status of the Magnetic Levitation Upgrade to the Holloman High Speed Test Track, 21st Aerodynamic Measurement Technology and Ground Testing Conference, 2000, pp. 2289.

[20] Gurol, H., Ketchen, D., Holland, L., Minto, D., Hooser, M., and Bosmajian, N., Status of the Holloman High

Speed Maglev Test Track (HHSMTT), AIAA Aviat 2014 - 30th AIAA Aerodyn Meas Technol Gr Test Conf (June), 2014, pp. 1–15. Doi: 10.2514/6.2014-2655.

[21] Chen, S., He, Y., and Li, Z., Analysis of the Rocket Sled Track Irregularity in Time and Frequency Domains, CICTP 2014: Safe, Smart, and Sustainable Multimodal Transportation Systems, 2014, pp. 111–8.

[22] Turnbull, D., Hooser, C., Hooser, M., and Myers, J., Soft Sled Test Capability at the Holloman High Speed Test Track. US Air Force T&E Days, 2010.

[23] Kevin Dunshee Holloman High-Speed Test Track Design Manual. vol. 1.

[24] Bashash, S., Salehi-Khojin, A., and Jalili, N., Forced Vibration Analysis of Flexible Euler-Bernoulli Beams with Geometrical Discontinuities, Proceedings of the American Control Conference, 2008.

[25] Xiang, J., He, D., and Zeng, Q. Y., Analysis Theory of Spatial Vibration of High-Speed Train and Slab Track System, J Cent South Univ Technol (English Ed, 2008. Doi: 10.1007/s11771-008-0024-9.

[26] Gao, F., Wu, Z., Li, F., and Zhang, C., Numerical and Experimental Analysis of The Vibration and Band-Gap Properties of Elastic Beams with Periodically Variable Cross Sections. Waves in Random and Complex Media, 2019. Doi: 10.1080/17455030.2018.1430918.

[27] Mosavi, A., Benkreif, R., and Varkonyi-Koczy, A. R., Comparison of Euler-Bernoulli and Timoshenko beam Equations for Railway System Dynamics, Advances in Intelligent Systems and Computing, 2018.

[28] Afshar, N. P., Samani, F. S., and Molaie, M., Application of Linear And Nonlinear Vibration Absorbers For The Nonlinear Beam Under Moving Load, J Comput Appl Res Mech Eng, 2015. Doi: 10.22061/jcarme.2015.344.

[29] Jin, L., Zhang, Q., Lei, B., and Li, Z., Simulation and Research on 3D Gouging Model Based on Abaqus/Explicit, 2012 16th International Symposium on Electromagnetic Launch Technology, 2012, pp. 1–5.

[30] Buentello Hernandez, R. G., Palazotto, A. N., and Le, K. H., 3D Finite Element Modeling of High-Speed Sliding Wear, Collect Tech Pap - AIAA/ASME/ASCE/AHS/ASC Struct Struct Dyn Mater Conf1–20, 2013.

[31] Greenwood, D. T., Advanced Dynamics Najafi MR, Moghadas SM Investigation Effect of Adding a SBR Damper to A Sled Sample and Extraction of Its Equivalent Stiffness and Damping. ADMT J, 2022.

[32] Carlson, H. W., Gapcynski, J. P., An Experimental Investigation at a Mach Number of 2.01 of the Effects of Body Cross-Section Shape on the Aerodynamic Characteristics of Bodies and Wing-Body Combinations, 1955.

[33] Cengel, Y. A., Fluid Mechanics, Tata McGraw-Hill Education.